communications earth & environment

Article

https://doi.org/10.1038/s43247-024-01878-7

Drying of the Martian mesosphere during aphelion induced by lower temperatures

Daniel Toledo[1] ✉, Pascal Rannou[2], Victor Apéstigue[1], Raul Rodriguez-Veloso[1], Ignacio Arruego[1], German Martínez[3], Leslie Tamppari[4], Asier Munguira[5], Ralph Lorenz[6], Aurélien Stcherbinine[7], Franck Montmessin[8], Agustin Sanchez-Lavega[5], Priya Patel[4], Michael Smith[9], Mark Lemmon[10], Alvaro Vicente-Retortillo[11], Claire Newman[12], Daniel Viudez-Moreiras[11], Ricardo Hueso[5], Tanguy Bertrand[13], Jorge Pla-Garcia[11], Margarita Yela[1], Manuel de la Torre Juarez[4] & Jose Antonio Rodriguez-Manfredi[11]

The formation of water ice clouds or hazes on Mars imposes substantial limitations on the vertical transport of water into the middle-upper atmosphere, impacting the planet's hydrogen loss. Recent observations made by the Mars Environmental Dynamics Analyzer instrument onboard Mars 2020 Perseverance rover have shown a marked decline in water ice abundance within the mesosphere (above 35-40 km) when Mars is near its aphelion (near the northern summer solstice), notably occurring during solar longitudes (Ls) between Ls 70° and 80°. Orbital observations around the same latitudes indicate that temperatures between ~ 30-40 km reach a minimum during the same period. Using cloud microphysics simulations, we demonstrate that this decrease in temperature effectively increases the amount of water cold-trapped at those altitudes, confining water ice condensation to lower altitudes. Similarly, the reinforcement of the cold trap induced by the lower temperatures results in significant reductions in the water vapor mixing ratio above 35–40 km, explaining the confinement of water vapor observed around aphelion from orbiters.

Geomorphological and geochemical evidence suggests that Mars, often considered a dry and arid planet, once harbored abundant water on its surface. Based on Mars's current water inventory and the isotopic fractionation observed, it is estimated that the planet has lost more than 85% of its original water reservoir to space[1]. Despite this significant loss, Mars still retains critical water reservoirs, including surface ice (e.g., the polar caps), subsurface ice in equilibrium with the atmospheric vapor or in diffusive contact with the atmosphere, and water molecules attached to the regolith[2]. Each of these reservoirs can be thermally activated, resulting in exchanges of water with the atmosphere and thereby contributing to the planet present-day water cycle[3–7]. In the equatorial regions between ~10°S and ~30°N, the primary source of atmospheric water vapor is the sublimation of the polar ice caps, especially the northern polar cap. During the Martian summer in the northern hemisphere, the ice in the polar cap sublimates, releasing water vapor into the atmosphere. This water vapor is then transported southward into the rising branch of the Hadley cell, where it cools and condenses.

While certain aspects of the process by which Mars lost its water remain unclear, it is well established that the planet's rate of water loss is significantly influenced by the supply of H_2O from the lower atmosphere to altitudes above ~60 km[8,9]. A key factor in this is the efficiency with which water is cold-trapped with altitude through condensation. Indeed, for condensable gases, the local mixing ratios should be limited to the values imposed by the Clausius-Clapeyron relation. Thus, an increase in cloud activity in a particular region should, in principle, not only limit the supply of H_2O to high altitudes (above 60 km) but also its cross-hemispheric transport. Conversely, a decrease in cloud activity, whether due to rising temperatures[10] or the inhibition of condensation by the absence of cloud

[1]Instituto Nacional de Técnica Aeroespacial (INTA), Madrid, Spain. [2]GSMA, UMR 7331-GSMA, Universite de Reims Champagne-Ardenne, 51687 Reims, France. [3]Lunar and Planetary Institute, Universities Space Research Association, Houston, TX, USA. [4]Jet Propulsion Laboratory, CAlifornia Institute of Technology, Pasadena, CA, USA. [5]Universidad del País Vasco UPV/EHU, Bilbao, Spain. [6]Johns Hopkins Applied Physics Laboratory, Laurel, MD, USA. [7]IRAP - Institut de Recherche en Astrophysique et Planétologie, Toulouse, France. [8]Laboratoire Atmosphères Milieux Observations Spatiales (LATMOS), Universitá Paris-Saclayz, Sorbonne Universitá, Centre National de la Recherche Scientifique, Guyancourt, France. [9]NASA Godard Space Flight Center, Greenbelt, MD, USA. [10]Space Science Institute, Boulder, CO, USA. [11]Centro de Atrobiología (INTA-CSIC), Torrejón de Ardoz, Madrid, Spain. [12]Aeolis Research, Chandler, AZ, USA. [13]LESIA, Observatoire de Paris, Meudon, France. ✉e-mail: toledocd@inta.es

condensation nuclei (CCN)[11] or other factors[12], should result in higher concentrations of water at high altitudes.

To gain insights into how water ice clouds (as liquid water clouds are not expected to form due to the pressure and temperature conditions) regulate the humidity of air entering the atmosphere at altitudes above 35–40 km, we analyzed ground-based data obtained during twilight (sunrise and sunset periods) from the Radiation and Dust Sensor (RDS)[13], which is part of the MEDA (Mars Environmental Dynamics Analyzer) instrument[14,15] onboard the NASA Perseverance rover (18.4°N 77.6°E). Additionally, we analyzed data from the solar arrays of Insight lander[16] (4.5°N 135.9°E) for the same period of the day. MEDA-RDS measures the solar irradiance at different spectral bands and geometries of observation (for this study, only the intensity at the zenith is utilized), while solar array photocurrents are linearly related to the Solar flux incident onto the semiconductor (Methods). As demonstrated in ref. 17, the solar irradiance at the surface during twilight and its variation with the solar zenith angle (SZA) is very sensitive to the presence of aerosol layers above ~35 km. Thus, we can evaluate the presence of high aerosol layers during twilight by comparing the variation of the signals with SZA to the characteristic variation observed when no high aerosol layers are present.

Results and discussion

For the Mars 2020 and Insight landing sites, Fig. 1a displays the sub-seasonal variation for various Martian Years (MY) of the slope derived from the correlation between signals measured under high-altitude-aerosol-free conditions (referred to as the reference signal) and the rest of the signals acquired during twilight at a certain Ls. Slope values significantly smaller than 1 (thresholds estimated to be ~0.97 for MEDA-RDS data and ~0.90 for InSight solar arrays) indicate the presence of high-altitude aerosol layers (water ice or dust), while values close to 1 or greater indicate high-altitude-aerosol-free conditions (Methods). Both datasets exhibit a similar seasonal variation and in consecutive MYs: slopes are significantly smaller than 1 between Ls ~30°–60° and Ls ~100°–140°. Given that this corresponds to the Aphelion Cloud Belt season[3], we infer that these slope variations are caused by the presence of water ice layers and at altitudes above 35 km[17]. This is consistent with the greater values of the color index (ratio between Top 4 and Top 8 channels) recorded during this period compared to the dusty season[17]. Thereafter, the clouds detected above ~35 km are referred to as mesospheric clouds in this study to distinguish them from the primary water ice tropospheric clouds found at altitudes ~10–20 km. In both datasets, we also observe slopes close to 1 at Ls ~80°, suggesting a decrease in the mesospheric cloud activity during this period at these two locations. The observation of this decline across different MYs and locations suggests a strong seasonal component.

Using a radiative transfer model (Methods), the cloud altitude, opacity (throughout the manuscript, opacity refers to optical depth), and particle radius were estimated for the MEDA-RDS observations (a similar analysis could not be conducted with the solar array data due to their broad spectral band). Fig. 1b shows the cloud opacities retrieved for MYs 36[17] and 37 during the cloudy period (cloud altitude and particle radius are given in Supplementary Fig. 1). Most of the cloud altitudes were found to be between 40 and 50 km, with particle radii ~1 μm. Fig. 1b not only shows a decrease in mesospheric cloud activity around aphelion (Ls ~70°–80°), but also a decrease in cloud opacity as we move to Ls values close to 80°. Interestingly,

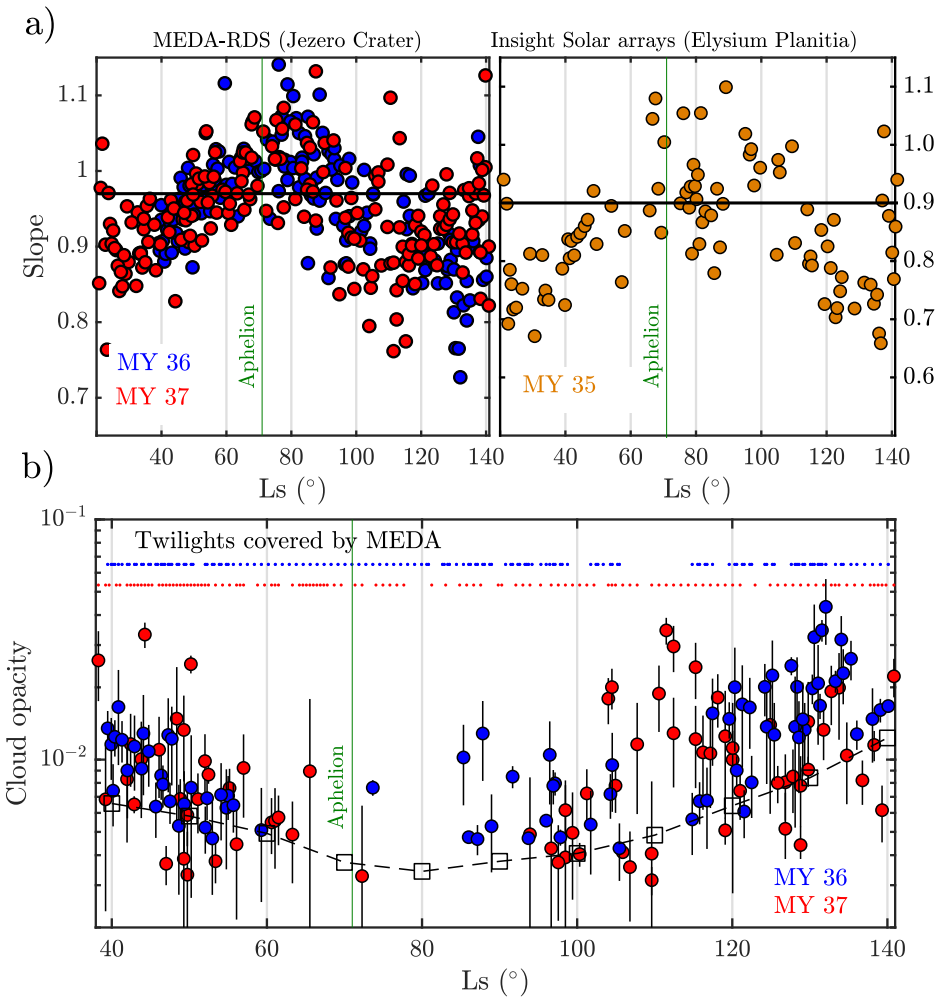

Fig. 1 | Seasonal variability of mesospheric H_2O ice clouds during the cloudy season. a Slopes derived from the correlation between signals measured for a cloud-free day (reference signal) and those covering twilight during the cloudy season (Methods). The vertical green line indicates the moment when Mars is at aphelion (Ls = 71°). For the slope analysis using MEDA-RDS, observations were made at 950 nm and for MYs 36 and 37 (left panel). For Insight solar array analysis, data acquired during sunset and for MY 35 were used (right panel). When comparing signals to estimate the slope, it is essential to ensure that they correspond to similar SZAs. Therefore, in each correlation, both signals are interpolated to the same SZA grid. As detailed in the Methods section, the reference signal is represented on the *x* axis for the slope estimation. Consequently, a slope smaller than 1 indicates higher signal intensities at twilight compared to the reference signal, suggesting the presence of high-altitude aerosol layers (assumed to be H_2O ice during the cloudy season). The horizontal black solid lines show the 0.97 and 0.90 threshold values. **b** Retrievals of cloud opacity derived from radiative transfer modeling of the MEDA-RDS observations at 450 and 950 nm (Methods) (blue and red circles with errors). The blue and red dots indicate the twilights during which MEDA-RDS measurements covered the solar zenith angle range SZA = [91°–97°] (required for the radiative transfer analysis). In most cloud detections, the cloud altitudes were found to be between 40 and 50 km. The figure also displays the cloud opacity above 35 km (dashed black line with squares) as derived from the microphysical simulations described below.

this decline in cloud opacity was not present in the column aerosol opacities retrieved at the same location and time from the MEDA Thermal Infrared Sensor (TIRS)[18]. This indicates that the reduction in cloud activity during aphelion occurs only at altitudes above 35 km, as MEDA-RDS observations at twilight are sensitive only to aerosol layers above that height, and the mesospheric cloud opacity accounts for only about 4% of the total aerosol column opacity retrieved from MEDA-TIRS. These results are also consistent with the vertical profiles of aerosol extinction retrieved from the Mid-InfraRed channel of the Atmospheric Chemistry Suite (ACS) instrument aboard the ExoMars Trace Gas Orbiter (TGO)[19], utilizing the procedure described in ref. 20,21, within the 0–40°N latitude band and for the same period and MYs as in Fig. 1 (see Supplementary Fig. 2). In particular, the ACS retrievals indicate lower water ice opacities around aphelion at altitudes above 35–40 km.

To determine the factors controlling the observed sub-seasonal variability of the mesospheric clouds, we simulated clouds using a one-dimensional cloud microphysical model previously employed for Titan[22] and Mars[5,23] (Methods). This model includes nucleation, condensation, coagulation, evaporation, precipitation, and coalescence. The vertical transport of H_2O gas is parameterized using an eddy-diffusion profile, which regulates the gas supply for cloud nucleation and particle growth. Based on prior studies[23–25], our baseline profile maintains a constant value of the eddy coefficient $K_{eddy} = 200\ m^2\ s^{-1}$ from the surface up to an altitude of 20 km. Beyond this altitude, K_{eddy} increases inversely with density towards the atmospheric top, set at 60 km. Various $K_{eddy}(z \le 20\ km)$ values were examined in simulations, and their impact on cloud formation results are discussed below. The model is run in cycles of one sol, utilizing diurnal temperature profiles derived from the Mars Climate Database (MCD)[26], version 6.1, and climatology scenario. Initial profiles of H_2O and CO_2 are also obtained from the MCD, with their vertical transport in the simulations determined by the eddy mixing profile (and for H_2O also by cloud precipitation). In the microphysical model, heterogeneous nucleation is assumed, with dust particles acting as CCNs. The initial dust profile follows an exponential decay with altitude, and its vertical transport is primarily influenced by eddy mixing and settling velocities. Consequently, the only constraint in the model is maintaining consistency with the MCD diurnal temperature profiles corresponding to the Ls values targeted for simulation.

Figure 2a, b show the variation of the vertical profiles and total column H_2O ice opacity with Ls derived from our microphysical model. Consistent with the findings depicted in Fig. 1, the model indicates a decrease in H_2O ice opacities above 35 km at Ls ~80°. Two distinct cloud layers are clearly discernible: one between 10 and 20 km altitude (tropospheric cloud), and another cloud layer above 20 km, with its total opacity being approximately one order of magnitude smaller than that of the tropospheric cloud. This difference in cloud opacity makes it difficult to study variations in mesospheric cloud activity through measurements of column aerosol opacity, emphasizing the necessity of utilizing twilight observations. In addition to reproducing the decline in the mesospheric cloud activity at Ls ~80° and the subsequent increase after Ls ~100°, the model provides H_2O ice opacities comparable to those retrieved from MEDA-RDS measurements (Fig. 1b). The simulated seasonal variability of the tropospheric cloud is also supported by measurements of column aerosol opacity retrieved from MEDA-TIRS[18] (Fig. 2c). Indeed, results from our model and TIRS retrievals exhibit a maximum in opacity at Ls between 100° and 110°. Although MEDA-TIRS aerosol opacities also include dust (hence the offset between the simulation curves, which only include ice, and the MEDA-TIRS measurements), it is expected that during the cloudy season and at sunrise, H_2O ice is the primary aerosol component influencing the seasonal aerosol opacity variability.

Different factors, such as variations in vertical mixing or temperatures, can contribute to the decrease in cloud activity in the mesosphere observed around Ls = 80°. Figure 2c demonstrates that a decrease in K_{eddy} results in smaller H_2O ice opacities. Therefore, a reduction in K_{eddy} with time around aphelion may explain the decline in mesospheric cloud opacities reported in Fig. 1. However, such a decrease would affect both tropospheric and mesospheric clouds by reducing their opacities, which contradicts observations. Indeed, MEDA-TIRS column opacity measurements do not show any slowing of increase or even decrease around aphelion. This suggests that even if the vertical mixing may vary across the cloudy season, these variations cannot be responsible for the decline in the mesospheric cloud activity. This is further supported by the simulations reported in Fig. 2b, which indicate that the decrease in H_2O ice opacity above 35 km occurs at Ls values during which the opacity of the tropospheric cloud is increasing. Thus, the mesospheric cloud opacity may decrease even without any decrease in K_{eddy}.

We conducted several tests in our simulations and identified temperatures between 30–40 km as the primary factor influencing the mesospheric cloud variability reported in Figs. 1 and 2. Specifically, the temperatures obtained from the MCD and utilized in our simulations exhibit a minimum around aphelion (see Supplementary Fig. 3). This minimum is also supported by the temperatures retrieved from the Mars Climate Sounder (MCS)[27,28] onboard the Mars Reconnaissance Orbiter, as shown in Fig. 3a, b and in Supplementary Fig. 4. Our simulations indicate that the decrease in temperature at altitudes between ~30 and 40 km around aphelion leads to lower saturation vapor pressures, requiring less H_2O vapor to reach saturation. As a consequence, more H_2O becomes cold-trapped at those altitudes, while less H_2O vapor is transported to the mesosphere, as H_2O vapor typically cannot surpass the saturation vapor pressure. To show this, Figs. 3c, d illustrates the influence of decreasing temperatures on the vertical profile of H_2O ice at sunrise. Different temperature perturbations, selected based on MCS temperature retrievals (see Supplementary Fig. 4), were added to all the daily MCD temperature profiles employed in the microphysical simulations (Figs. 3c). The simulations shown in Figs. 3d indicate that the temperature decreases around aphelion, as obtained from MCS (with minimum values reaching between −10 and −15 K), is significant enough to cause a reduction in water ice opacity above 35 km by a factor of ~0.4, which is on the same order as the water ice opacity reduction reported from MEDA-RDS retrievals. Similarly, these simulations show that the temperature decrease as we approach aphelion is expected to have contrasting effects on tropospheric and mesospheric clouds, as we saw in Fig. 2d. Similar simulations but for the daily average (shown in Supplementary Fig. 5) indicate a reduction in the ice opacity above 35 km by ~55–65% as a result of the temperature decrease derived from MCS.

However, it is important to note that the formation of clouds requires the presence of dust particles (or CCNs) for heterogeneous nucleation. Without the presence of dust, vapor saturation can reach high levels without cloud formation, which prevents any restriction on the amount of vapor being transported upward. This may explain the high saturation levels, with values up to 10, observed by orbiters[11]. Similarly, recent observations have revealed regions in the Martian atmosphere that are supersaturated while also containing dust particles (or CCNs)[12,29]. One possible explanation is that the saturation is not reaching values high enough to achieve sufficient nucleation (~1 embryo $cm^2\ s^{-1}$) to produce clouds. This saturation, defined as the critical saturation (S_{crit}), depends on various factors such as the radius of the CCNs or the temperature. We found that at altitudes between 30 and 40 km, and for a CCN radius of 0.1 μm, S_{crit} is between 1.8 and 2. For smaller CCN radii, S_{crit} is expected to take greater values (e.g., for a radius of 0.01 μm, S_{crit} increases to values between 2.5 and 3 at those altitudes). Therefore, the extent to which the presence of clouds restricts the vertical transport of H_2O vapor depends on the values of S_{crit}, which in turn depends on factors such as the CCN properties, temperature, and pressure.

Cloud simulations also indicate that the reinforcement of the cold trap, induced by the lower temperatures, should affect not only the concentration of H_2O ice in the mesosphere but also the water vapor content. Recent analyses of the measurements made by the Nadir and Occultation for Mars Discovery (NOMAD) instrument[30] onboard ExoMars TGO show a pronounced decrease in the H_2O vapor abundance in the high troposphere-mesosphere at Ls values close to aphelion[31]. Figure 4 illustrates a comparison between the H_2O vapor volume mixing ratio (VMR) retrieved from NOMAD[31] in MY 35 (brown) and MY 36 (green) at four different altitudes (a-d) and latitudes between −30° and 30°, along with the daily average

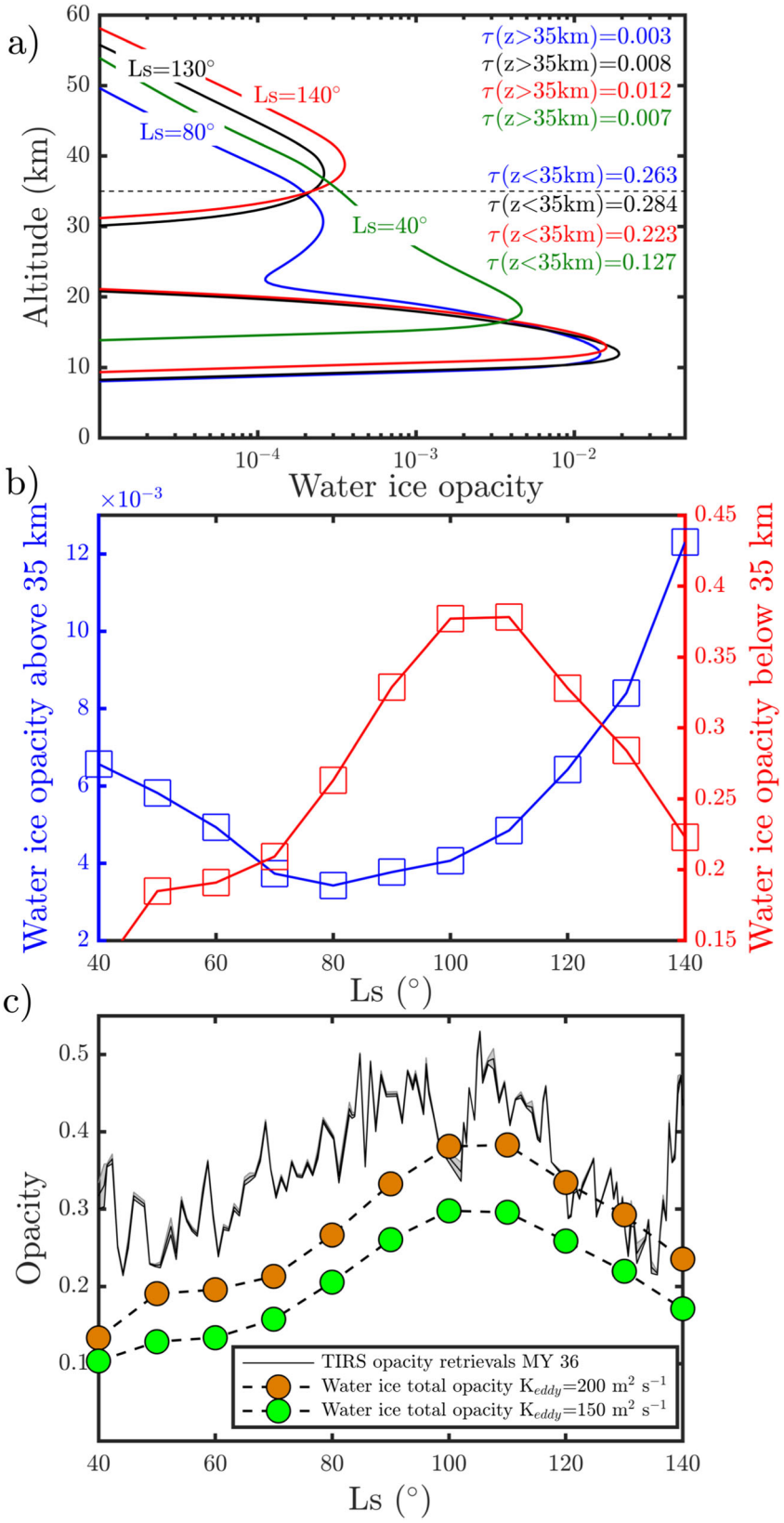

Fig. 2 | Numerical simulations of H_2O ice clouds. **a** Vertical profiles of H_2O ice opacity (τ) at sunrise obtained with the microphysical model for Ls=40° (green line), 80° (blue line), 130° (black line), and 140° (red line). The black dashed line indicates the 35 km altitude, approximately representing the minimum altitude for cloud detection using the MEDA-RDS observations. **b** Variation of H_2O ice opacity at sunrise above (blue line and left *y* axis) and below (red line and right *y* axis) 35 km with Ls. **c** Comparison of the variation in aerosol opacity (clouds and dust) retrieved from the MEDA-TIRS instrument[18] and the total column H_2O ice opacity obtained from the microphysical model, both at sunrise. These simulations employed two different values of K_{eddy} below 20 km to show the impact of this parameter on the simulations. In general, within the expected range of K_{eddy} values for Mars, variations in K_{eddy} ($z \leq 20$ km) affect the total H_2O ice opacity. The seasonal variability of the total H_2O column ice opacity is primarily dominated by the tropospheric cloud due to its higher opacity compared to the mesospheric clouds.

results obtained from the microphysical model for our baseline run (dashed black line). Each simulation uses the values provided by the MCD as the initial H_2O profile at the targeted Ls and the Perseverance landing coordinates. In order to investigate the impact of this initial H_2O abundance on the model results, Fig. 4 also displays the same simulations but uses the same initial H_2O profile for all Ls (purple dashed lines). In Fig. 4, we see some short-term variability in the NOMAD VMR retrievals, which cannot be reproduced by the model. Such variations may arise from multiple factors, including latitudinal and longitudinal variations in H_2O vapor VMR that our one-dimensional model fails to capture (since the model is run in a single location as described in Methods), the local time of TGO observations, or possible variations produced by gravity wave activity[32,33].

Nevertheless, the model reasonably reproduces the seasonal variation of H_2O vapor VMR retrieved from NOMAD, indicating a minimum of around the same Ls values. Although some variations are observed in the two model scenarios (black and purple dashed lines in Fig. 4), they fall within the error bars. This suggests that variations in the total H_2O abundance are not the primary factor controlling the seasonality of H_2O vapor VMR in the mesosphere. Similar to the analysis for H_2O ice, we evaluated the impact of adding the temperature perturbation obtained from MCS data

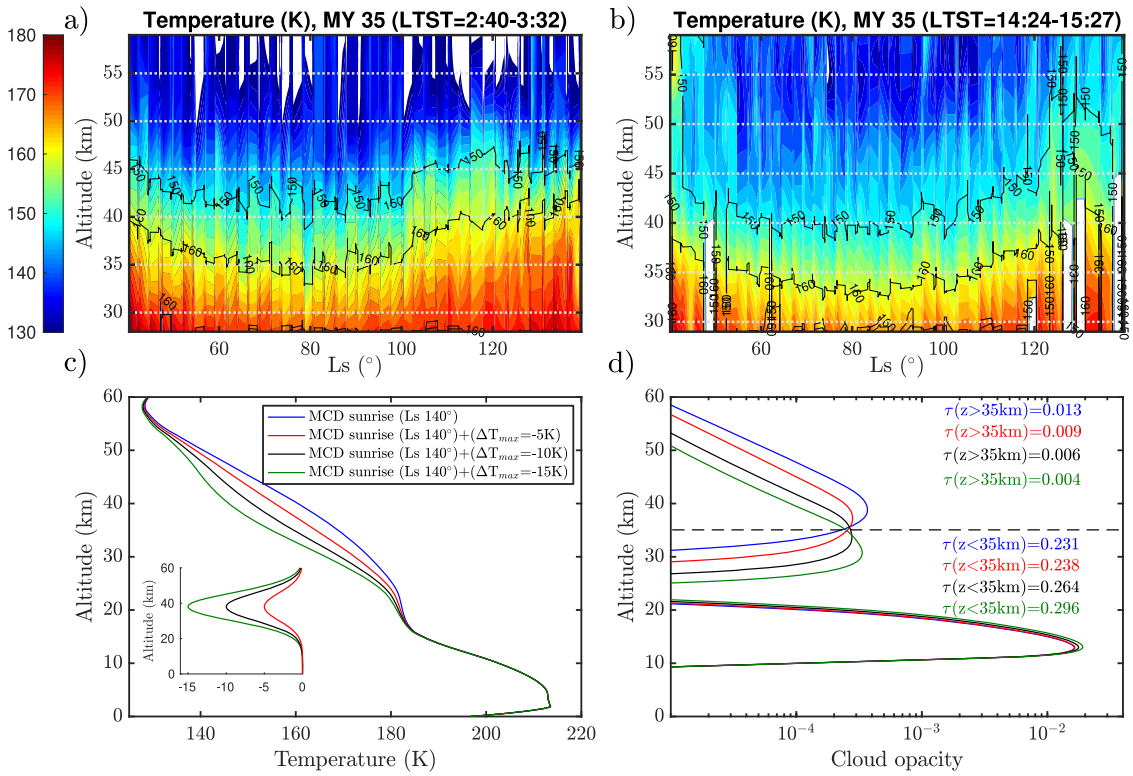

Fig. 3 | The seasonal variability of H_2O mesospheric clouds is largely influenced by tropospheric temperatures. a, **b** MCS temperature retrievals at two time intervals for MY 35 near the Perseverance landing site. **c** Temperature profiles tested in the simulations. The baseline profile (blue solid line) is taken from the MCD for Ls = 140°. The rest of profiles are derived by adding to the baseline profile the temperature perturbations (ΔT) shown in the inset figure, whose parametrization is based on the MCS data (see Supplementary Fig. 4). **d** H_2O ice profiles at sunrise were obtained with the microphysical model using the temperature profiles shown in (**c**). For a given temperature perturbation, ΔT is added to all the daily cycles of temperature profiles corresponding to Ls = 140°.

Fig. 4 | Observations and numerical simulations of H_2O vapor. Comparison between the variation of H_2O vapor volume mixing ratio (VMR) with Ls retrieved from ExoMars TGO/NOMAD[31] for MY 35 (brown dots) and 36 (green dots) and the daily average model results at altitudes of 30 (**a**), 35 (**b**), 40 (**c**), and 45 (**d**) km. The black error bars depict the model results under baseline model conditions (the errors represent the daily standard deviation of VMR), while the purple error bars represent the results when using the same initial H_2O vapor VMR profile (the one corresponding to Ls = 40°) for all Ls. In both model scenarios, the temperatures are constrained to follow the daily temperature cycle of the Mars Climate Database corresponding to the Ls simulated. For this comparison, only NOMAD retrievals at latitudes between −30° and 30° were considered.

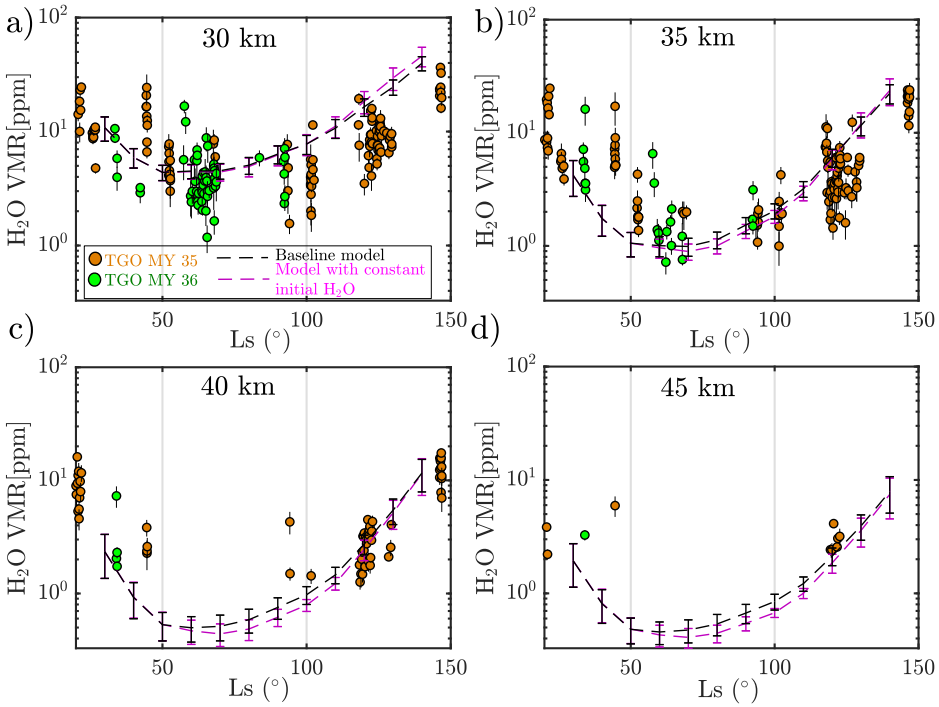

(Supplementary Fig. 4) on the daily average H_2O vapor VMR, with the results shown in Supplementary Fig. 6. These simulations indicate that a temperature variation between −10 and −15 K at altitudes between 30 and 40 km can result in a decrease in H_2O vapor VMR at 60 km of up to 78–90%. Therefore, these simulations demonstrate the strong impact of the cold trap on the vertical distribution of both H_2O vapor and ice in the mesosphere.

This connection between temperatures and the abundance of H_2O in the mesosphere has significant implications for Mars water cycle. Based on the strong response of hydrogen loss to the presence of water at high altitudes (above ~60 km)[34–36], further supported by photochemical simulations[8,9,37], it has been established that H_2O transport to high altitudes is likely the main contributor in the hydrogen escape rate of the planet, rather than the production of molecular hydrogen in the lower atmosphere and its subsequent slow diffusion. Indeed, water vapor transported directly to altitudes above ~60 km dissociates into atomic hydrogen, and atoms with sufficient velocity can be lost to space. This conclusion is further supported by observed seasonal variations in hydrogen escape rates[38–40], as well as by general circulation models[41,42]. However, if the water vapor is confined to lower altitudes, as reported during aphelion, molecular hydrogen is expected to be the main precursor of H atoms[43], resulting in hydrogen escape rates that are approximately 10–100 times lower[44]. MEDA ground-based observations reported in this work, along with orbital observations and modeling, show a rapid response in the mesospheric water content to temperature variations between ~30–40 km. Such variations have a strong orbital component during the analyzed period. During the Martian aphelion (Ls ~70°–80°), the solar flux received by the planet is approximately 40% less than that at perihelion, resulting in annual temperature variations that can be up to ~20 K[45]. As depicted in Fig. 3 and Supplementary Figs. 5–6, these temperature variations are sufficient to result in a significant decrease in mesospheric water abundance. Thus, the heliocentric distance between the Sun and Mars may influence hydrogen escape rates, not only through variations in incident ultraviolet light but also by possibly reinforcing the tropospheric cold trap. However, more work is needed to determine the spatial extent (latitude and longitude) to which the MEDA-RDS observations are applicable, particularly the decline in cloud activity around aphelion. Indeed, although the MEDA-RDS measurements seem consistent with the observations carried out by orbiters (e.g., the ice measurements by TGO/ACS provided in Supplementary Fig. 2) and InSight solar panels, it is important to note the local nature of the main observations used in this work.

Reduced dustiness also contributes to cooler atmospheric temperatures, typically marking the aphelion season as the annual minimum in dust opacity. Previous works have demonstrated year-to-year temperature variability at aphelion of up to 15–20 K in the 0–60 km altitude region[3], associated with variations in the dust cycle. The sensitivity of the mesospheric water content to temperature, as reported in this work, suggests that these temperature variations might have contributed to fluctuations in water content at high altitudes, which could have had some impact on the planet's hydrogen loss. Present-day escape rates are approximately one order of magnitude or more below the value required to account for the total water lost from the planet initial reservoir[35,46]. Variations in the dust cycle may explain this discrepancy, or variations in the planet orbit and obliquity, which occur over longer timescales, might also play a role. Global circulation simulations indicate warmer temperatures and wetter conditions at high obliquity[47]. Given that the planet long-term average obliquity exceeds the present value[48], it is reasonable to consider greater hydrogen escape rates in the recent past of the planet. However, more work is needed to determine the extent to which higher concentrations of water vapor in the middle-upper atmosphere can increase the planet H loss, as recent studies suggest that in the long term, the escape rate of hydrogen may eventually be limited by the recombination of H and O back to H_2O[46].

Methods

MEDA-RDS data processing

The MEDA-RDS includes two sets of eight photodiodes and a camera (SkyCam)[13,14]. One set of photodiodes is directed upward (referred as Top channels), each covering a distinct wavelength range from 190 to 1200 nm. The other set is positioned sideways, 20 degrees above the horizon, and spaced 45 degrees apart in azimuth to sample all directions at a single wavelength. In this work, only the observations made by Top 4 (450 ± 10 nm) and Top 8 (950 ± 10 nm) channels are considered. The MEDA-RDS sampling rate is set at 1 Hz, with all sensors operating normally in blocks of 1 hour. The arrangement of the blocks throughout the day is selected for each Martian sol based on a cadence that alternates between even and odd hours. The number and duration of blocks may vary depending on power availability and data volume constraints. As a result, not all twilights are covered by MEDA-RDS. For the slope analysis (Supplementary Fig. 7) and the radiative transfer simulations, the signals are normalized to their corresponding values at the SZA closest to 90°. This normalization reduces the influence of dust opacity and particle radius on the RDS signals, making the comparison between signals easier to interpret.

Insight solar arrays data processing

For the Insight data analysis, only twilights with SZA ranging between 90° and 96° were considered to ensure sensitivity to high-altitude aerosol layers. Typically, the intensities at sunrise were notably lower than those at sunset and did not fall within this SZA range. The exact reason for this discrepancy is unclear, but it may be associated with temperature effects or possible shadows. Consequently, sunrises were excluded from the study. Additionally, due to intensity attenuation caused by accumulated dust, only data from Martian Year 35 (MY 35) could be included in the analysis. Supplementary Fig. 8 illustrates an example of the variation in solar array currents measured during twilight for two different sols and their correlation analysis for two different scenarios of aerosols. Similarly to the MEDA-RDS data, the signals were normalized to their corresponding values at the SZA closest to 90°.

Radiative transfer model

The radiative transfer simulations were performed using a Monte-Carlo radiative transfer code, which has been previously employed for modeling clouds on Mars, Titan, and Earth[17,49–51]. The model is in spherical geometry as the simulations are conducted for SZA > 90°. For the aerosol properties, we used the model described in ref. 17. The cloud altitude, number density, and particle size are determined by fitting the Top 4 (450 nm) and Top 8 (950 nm) twilight observations simultaneously. The cloud opacity at each wavelength is obtained from the fitted cloud number density and the particle cross-section, which is calculated using Mie theory, the fitted effective radius (r_{eff}), and the refractive index of H_2O ice. Only the twilights for which the RDS observations covered the minimum SZA range of [91°–97°] are analyzed with the model. Dust opacity (τ) vertical profiles were characterized using the modified Conrath profile:

$$\tau(z) = \tau_0 \cdot \sigma(z) \cdot \exp\left[\nu \cdot \left(1 - \sigma(z)^{-l}\right)\right] \quad (1)$$

where τ_0 is the vertical opacity at surface, ν is a constant set to 0.007, $\sigma(z)$ is the ratio between the pressure at z level and the pressure at surface, and l is the ratio between a reference height (set to 70 km) and the altitude of the top of the dust layer. Assuming no detached dust layers are present above 25 km during the cloudy period, we designated the altitude of the top of the dust layer at 45 km. Ref. 17 indicates that varying this parameter from 30 to 50 km does not result in significant differences in the cloud retrievals.

Cloud microphysics model

The microphysical scheme follows the same approach as that used in the LMD-GCM model, which has been previously described in refs. 5,23,52–54; therefore, only the specifications relevant to this work are detailed. The model runs with 200 points equally spaced in altitude from 0 to 60 km, an aerosol distribution grid consisting of 30 size bins (assuming a logarithmic bin-size distribution), and a time-step of 6 minutes. The selection of this parameterization was based on a number of sensitivity tests of the results of the time-step altitude, and size grids. Each simulation is conducted over a daily cycle, with temperatures constrained to follow the MCD profiles

corresponding to the targeted Ls and, unless stated otherwise, the Perseverance landing site coordinates. The initial profile of H_2O vapor is also taken from the MCD, specifically the profile at 14:00 local time, which is around the time when the water ice column is at its minimum. Heterogeneous nucleation is assumed for the nucleation, being the dust particles the CCN. For the dust, we assumed a total opacity of 0.2 (based on ref. 18), an effective radius of 1.2 μm[55] in the simulations. The values of the parameters required to compute the nucleation and condensation rates, as well as the settling velocities, are taken from refs. 23,56, while the water saturation vapor pressure is computed according to ref. 57. We ran the model until a steady state in the cloud profiles is reached, typically occurring after 5–6 Martian days.

Data availability

All Perseverance data used in this study are publicly available via the Planetary Data System[58] (the direct link is https://pds-atmospheres.nmsu.edu/data_and_services/atmospheres_data/PERSEVERANCE/meda.html). The InSight solar array data are available on the NASA Planetary Data System (PDS) in the InSight Spacecraft Raw Engineering and Ancillary Data Collection in the insight-ifg-mars bundle held at the Planetary Plasma Interactions PDS Node https://pds-ppi.igpp.ucla.edu. The data to create the different figures of the paper is available in an archive located at (https://doi.org/10.5281/zenodo.13773098)[59].

Received: 3 May 2024; Accepted: 5 November 2024;
Published online: 20 November 2024

References

1. Carr, M. H. Water on Mars. *Nature* **326**, 30–35 (1987).
2. Wright, V., Morzfeld, M. & Manga, M. Liquid water in the martian midcrust. *Proc. Natl Acad. Sci.* **121**, e2409983121 (2024).
3. Clancy, R. et al. Water vapor saturation at low altitudes around Mars aphelion: a key to Mars climate? *Icarus* **122**, 36–62 (1996).
4. Tamppari, L. K., Zurek, R. & Paige, D. Viking-era diurnal water-ice clouds. *J. Geophys. Res. Planets* 108 (2003).
5. Montmessin, F., Forget, F., Rannou, P., Cabane, M. & Haberle, R. M. Origin and role of water ice clouds in the Martian water cycle as inferred from a general circulation model. *J. Geophys. Res. Planets* 109 (2004).
6. Smith, M. D. Interannual variability in tes atmospheric observations of mars during 1999–2003. *Icarus* **167**, 148–165 (2004).
7. Montmessin, F., Smith, M. D., Langevin, Y., Mellon, M. T. & Fedorova, A. The water cycle. *Atmos. Clim. Mars* **18**, 338–373 (2017).
8. Chaffin, M., Deighan, J., Schneider, N. & Stewart, A. Elevated atmospheric escape of atomic hydrogen from mars induced by high-altitude water. *Nat. Geosci.* **10**, 174–178 (2017).
9. Stone, S. W. et al. Hydrogen escape from Mars is driven by seasonal and dust storm transport of water. *Science* **370**, 824–831 (2020).
10. Fedorova, A. et al. Water vapor in the middle atmosphere of Mars during the 2007 global dust storm. *Icarus* **300**, 440–457 (2018).
11. Maltagliati, L. et al. Evidence of water vapor in excess of saturation in the atmosphere of Mars. *Science* **333**, 1868–1871 (2011).
12. Fedorova, A. A. et al. Stormy water on mars: the distribution and saturation of atmospheric water during the dusty season. *Science* **367**, 297–300 (2020).
13. Apestigue, V. et al. Radiation and dust sensor for Mars environmental dynamic analyzer onboard m2020 rover. *Sensors* **22**, 2907 (2022).
14. Rodriguez-Manfredi, J. A. et al. The mars environmental dynamics analyzer, meda. a suite of environmental sensors for the mars 2020 mission. *Space Sci. Rev.* **217**, 1–86 (2021).
15. Rodriguez-Manfredi, J. A. et al. The diverse meteorology of jezero crater over the first 250 sols of perseverance on mars. *Nat. Geosci.* **16**, 19–28 (2023).
16. Lorenz, R. D., Lemmon, M. T. & Maki, J. First mars year of observations with the insight solar arrays: winds, dust devil shadows, and dust accumulation. *Icarus* **364**, 114468 (2021).
17. Toledo, D. et al. Twilight mesospheric clouds in jezero as observed by meda radiation and dust sensor (rds). *J. Geophys. Res. Planets* **128**, e2023JE007785 (2023).
18. Smith, M. D. et al. Diurnal and seasonal variations of aerosol optical depth observed by meda/tirs at jezero crater, mars. *J. Geophys. Res. Planets* **128**, e2022JE007560 (2023).
19. Korablev, O. et al. The atmospheric chemistry suite (acs) of three spectrometers for the exomars 2016 trace gas orbiter. *Space Sci. Rev.* **214**, 1–62 (2018).
20. Stcherbinine, A. et al. Martian water ice clouds during the 2018 global dust storm as observed by the acs-mir channel onboard the trace gas orbiter. *J. Geophys. Res. Planets* **125**, e2019JE006300 (2020).
21. Stcherbinine, A. et al. A two martian years survey of water ice clouds on mars with acs onboard TGO. *J. Geophys. Res. Planets* **127**, e2022JE007502 (2022).
22. Rannou, P., Montmessin, F., Hourdin, F. & Lebonnois, S. The latitudinal distribution of clouds on titan. *Science* **311**, 201–205 (2006).
23. Montmessin, F., Rannou, P. & Cabane, M. New insights into martian dust distribution and water-ice cloud microphysics. *J. Geophys. Res. Planets* **107**, 4–1 (2002).
24. Michelangeli, D. V., Toon, O. B., Haberle, R. M. & Pollack, J. B. Numerical simulations of the formation and evolution of water ice clouds in the martian atmosphere. *Icarus* **102**, 261–285 (1993).
25. Colaprete, A., Toon, O. B. & Magalhães, J. A. Cloud formation under mars pathfinder conditions. *J. Geophys. Res. Planets* **104**, 9043–9053 (1999).
26. Forget, F. et al. Improved general circulation models of the martian atmosphere from the surface to above 80 km. *J. Geophys. Res. Planets* **104**, 24155–24175 (1999).
27. Kleinböhl, A. et al. Mars climate sounder limb profile retrieval of atmospheric temperature, pressure, and dust and water ice opacity. *J. Geophys. Res. Planets* **114** (2009).
28. Kleinböhl, A., Friedson, A. J. & Schofield, J. T. Two-dimensional radiative transfer for the retrieval of limb emission measurements in the martian atmosphere. *J. Quant. Spectrosc. Radiat. Transf.* **187**, 511–522 (2017).
29. Fedorova, A. et al. A two-martian years survey of the water vapor saturation state on mars based on acs nir/tgo occultations. *J. Geophys. Res. Planets* **128**, e2022JE007348 (2023).
30. Vandaele, A. C. et al. Nomad, an integrated suite of three spectrometers for the exomars trace gas mission: technical description, science objectives and expected performance. *Space Sci. Rev.* **214**, 1–47 (2018).
31. Aoki, S. et al. Global vertical distribution of water vapor on mars: results from 3.5 years of exomars-tgo/nomad science operations. *J. Geophys. Res. Planets* **127**, e2022JE007231 (2022).
32. Yiğit, E., Medvedev, A. S., Benna, M. & Jakosky, B. M. Dust storm-enhanced gravity wave activity in the martian thermosphere observed by maven and implication for atmospheric escape. *Geophys. Res. Lett.* **48**, e2020GL092095 (2021).
33. Shaposhnikov, D. S., Medvedev, A. S., Rodin, A. V., Yiğit, E. & Hartogh, P. Martian dust storms and gravity waves: disentangling water transport to the upper atmosphere. *J. Geophys. Res. Planets* **127**, e2021JE007102 (2022).
34. Clarke, J. T. et al. A rapid decrease of the hydrogen corona of mars. *Geophys. Res. Lett.* **41**, 8013–8020 (2014).
35. Heavens, N. G. et al. Hydrogen escape from mars enhanced by deep convection in dust storms. *Nat. Astron.* **2**, 126–132 (2018).
36. Chaffin, M. S. et al. Martian water loss to space enhanced by regional dust storms. *Nat. Astron.* **5**, 1036–1042 (2021).
37. Kleinböhl, A. et al. Hydrogen escape on mars dominated by water vapour photolysis above the hygropause. *Nat. Astron*. **8**, 1–11 (2024).
38. Chaffin, M. S. et al. Unexpected variability of martian hydrogen escape. *Geophys. Res. Lett.* **41**, 314–320 (2014).

39. Bhattacharyya, D., Clarke, J. T., Bertaux, J.-L., Chaufray, J.-Y. & Mayyasi, M. A strong seasonal dependence in the martian hydrogen exosphere. *Geophys. Res. Lett.* **42**, 8678–8685 (2015).
40. Halekas, J. Seasonal variability of the hydrogen exosphere of mars. *J. Geophys. Res.: Planets* **122**, 901–911 (2017).
41. Chaufray, J.-Y. et al. Variability of the hydrogen in the martian upper atmosphere as simulated by a 3d atmosphere–exosphere coupling. *Icarus* **245**, 282–294 (2015).
42. Chaufray, J.-Y. et al. Study of the hydrogen escape rate at mars during martian years 28 and 29 from comparisons between spicam/mars express observations and gcm-lmd simulations. *Icarus* **353**, 113498 (2021).
43. Montmessin, F. et al. Reappraising the production and transfer of hydrogen atoms from the middle to the upper atmosphere of mars at times of elevated water vapor. *J. Geophys. Res. Planets* **127**, e2022JE007217 (2022).
44. Chaffin, M. S. et al. Mars h escape rates derived from maven/iuvs lyman alpha brightness measurements and their dependence on model assumptions. *J. Geophys. Res. Planets* **123**, 2192–2210 (2018).
45. Clancy, R. T., Muhleman, D. O. & Berge, G. L. Global changes in the 0–70 km thermal structure of the mars atmosphere derived from 1975 to 1989 microwave co spectra. *J. Geophys. Res. Solid Earth* **95**, 14543–14554 (1990).
46. Jakosky, B. M. Atmospheric loss to space and the history of water on mars. *Annu. Rev. Earth Planet. Sci.* **49**, 71–93 (2021).
47. Madeleine, J.-B. et al. Recent ice ages on mars: the role of radiatively active clouds and cloud microphysics. *Geophys. Res. Lett.* **41**, 4873–4879 (2014).
48. Laskar, J. et al. Long term evolution and chaotic diffusion of the insolation quantities of mars. *Icarus* **170**, 343–364 (2004).
49. Toledo, D., Rannou, P., Pommereau, J.-P., Sarkissian, A. & Foujols, T. Measurement of aerosol optical depth and sub-visual cloud detection using the optical depth sensor (ods). *Atmos. Meas. Tech.* **9**, 455–467 (2016).
50. Toledo, D. et al. Measurement of dust optical depth using the solar irradiance sensor (sis) onboard the exomars 2016 edm. *Planet. Space Sci.* **138**, 33–43 (2017).
51. West, R. et al. Cassini imaging science subsystem observations of titan's south polar cloud. *Icarus* **270**, 399–408 (2016).
52. Toon, O. B., Turco, R., Westphal, D., Malone, R. & Liu, M. A multidimensional model for aerosols: description of computational analogs. *J. Atmos. Sci.* **45**, 2123–2144 (1988).
53. Cabane, M., Chassefiere, E. & Israel, G. Formation and growth of photochemical aerosols in titan's atmosphere. *Icarus* **96**, 176–189 (1992).
54. Rannou, P., Hourdin, F., Mckay, C. P. & Luz, D. A coupled dynamics-microphysics model of titan's atmosphere. *Icarus* **170**, 443–462 (2004).
55. Chen-Chen, H., Pérez-Hoyos, S. & Sánchez-Lavega, A. Dust particle size and optical depth on mars retrieved by the msl navigation cameras. *Icarus* **319**, 43–57 (2019).
56. Reid, R. C., Prausnitz, J. M. & Poling, B. E. The properties of gases and liquids (1987).
57. Fray, N. & Schmitt, B. Sublimation of ices of astrophysical interest: a bibliographic review. *Planet. Space Sci.* **57**, 2053–2080 (2009).
58. Rodriguez-Manfredi, J. A. & de la Torre Juarez, M. Mars 2020 perseverance rover mars environmental dynamics analyzer (meda) experiment data record (edr) and reduced data record (rdr) data products archive bundle [Dataset]. *PDS Atmos. Node* **10**, 1522849 (2021).
59. Toledo, D. Drying of the martian mesosphere during aphelion induced by lower tropospheric temperatures. https://doi.org/10.5281/zenodo.13773098 (2024).

Acknowledgements

This work has been funded by the Spanish Ministry of Science and Innovation through the grant PID2022-139386OA-I00. Part of this research has been carried out at the Jet Propulsion Laboratory, California Institute of Technology, under an STMD and SMD grant for MEDA-US and under a contract with the National Aeronautics and Space Administration (80NM0018D0004). M2020 and MEDA data are available at the Data Planetary System courtesy of NASA and the Jet Propulsion Laboratory. RL acknowledges the support of InSight Participating Scientist grant 80NSSC18K1626 and the Mars 2020 Project via contract 1655893 with the Jet Propulsion Laboratory. R.H., A.S.L., and A.M. were supported by Grant PID2019-109467GB-I00 funded by MCIN/AEI/10.13039/501100011033 and by Grupos Gobierno Vasco IT1742-22. A.M. was also supported by the grant PRE2020-092562 funded by MCIN/AEI/10.13039/501100011033 and by 'ESF Investing in your future'. The authors would also like to thank the anonymous reviewers for their numerous suggestions, which greatly improved the manuscript.

Author contributions

D.T. led the writing of the paper and the analysis of the data. P.R. provided support for the microphysics modeling. V.A., R.R.V., and I.A. supported the interpretation of the RDS data and the different analyses. G.M. contributed to the writing and data analysis. L.T. provided the MCS data and support for the analysis. A.M. assisted in data analysis and writing. R.L. provided support for the analysis of the solar array data. A.S. provided support to the paper's conclusions with the ACS retrievals. F.M. contributed to the microphysical modeling. A.S.L. and P.P. supported the interpretation of the cloud observations. M.S. contributed to the analysis, providing the TIRS retrievals. M.L., A.V.R., C.N., D.V.M., R.H., T.B., J.P.G., M.Y., M.T.J., and J.A.R.M. supported the interpretation of the results.

Competing interests

The authors declare no competing interests.

Additional information

Supplementary information The online version contains supplementary material available at https://doi.org/10.1038/s43247-024-01878-7.

Correspondence and requests for materials should be addressed to Daniel Toledo.

Peer review information *Communications Earth & Environment* thanks the anonymous reviewers for their contribution to the peer review of this work. Primary Handling Editor: Joe Aslin. A peer review file is available